

f-Electron and Magnetic Ordering Effects in Nickelates LaNiO₂ and NdNiO₂: Remarkable Role of The Cuprate-Like 3d_{x²-y²} Band

Jianwei Sun (✉ jsun@tulane.edu)

Tulane University <https://orcid.org/0000-0002-2361-6823>

Ruiqi Zhang

Tulane University <https://orcid.org/0000-0002-7820-6020>

Christopher Lane

Theoretical Division, Los Alamos National Laboratory

Bahadur Singh

Northeastern University Boston <https://orcid.org/0000-0002-2013-1126>

Johannes Nokelainen

LUT University

Bernardo Barbiellini

LUT University

Robert Markiewicz

Northeastern University

Arun Bansil

Northeastern University

Article

Keywords: NdNiO₂, nickelates, magnetic

Posted Date: October 7th, 2020

DOI: <https://doi.org/10.21203/rs.3.rs-76787/v1>

License:   This work is licensed under a Creative Commons Attribution 4.0 International License.

[Read Full License](#)

Version of Record: A version of this preprint was published at Communications Physics on June 7th, 2021. See the published version at <https://doi.org/10.1038/s42005-021-00621-4>.

f-electron and magnetic ordering effects in nickelates LaNiO₂ and NdNiO₂: remarkable role of the cuprate-like $3d_{x^2-y^2}$ band

Ruiqi Zhang,^{1,*} Christopher Lane,^{2,3} Bahadur Singh,⁴ Johannes Nokelainen,^{5,6}
Bernardo Barbiellini,^{5,6} Robert S. Markiewicz,⁶ Arun Bansil,^{6,†} and Jianwei Sun^{1,‡}

¹*Department of Physics and Engineering Physics,
Tulane University, New Orleans, LA 70118, USA*

²*Theoretical Division, Los Alamos National Laboratory, Los Alamos, New Mexico 87545, USA*

³*Center for Integrated Nanotechnologies, Los Alamos National Laboratory, Los Alamos, New Mexico 87545, USA*

⁴*Department of Condensed Matter Physics and Materials Science,
Tata Institute of Fundamental Research, Colaba, Mumbai 400005, India.*

⁵*Department of Physics, School of Engineering Science,
LUT University, FI-53850 Lappeenranta, Finland*

⁶*Department of Physics, Northeastern University, Boston, MA 02115, USA*

Recent discovery of superconductivity in the doped infinite-layer nickelates has renewed interest in understanding the nature of high-temperature superconductivity more generally. The low-energy electronic structure of the parent compound NdNiO₂, the role of electronic correlations in driving superconductivity, and the possible relationship between the cuprates and the nickelates are still open questions. Here, by comparing LaNiO₂ and NdNiO₂ systematically within a parameter free density functional framework, all-electron first-principles framework, we reveal the role Nd 4*f* electrons in shaping the ground state of pristine NdNiO₂. Strong similarities are found between the electronic structures of LaNiO₂ and NdNiO₂, except for the effects of the 4*f*-electrons. Hybridization between the Nd 4*f* and Ni 3*d* orbitals is shown to significantly modify the Fermi surfaces of various magnetic states. In contrast, the competition between the magnetically ordered phases depends mainly on the gaps in the Ni $d_{x^2-y^2}$ band, so that the ground state in LaNiO₂ and NdNiO₂ turns out to be striking similarity to that of the cuprates. The $d-p$ band-splitting is found to be much larger while the intralayer 3*d* ion-exchange coupling is smaller in the nickelates compared to the cuprates. Our estimated value of the on-site Hubbard U is similar to that in the cuprates, but the value of the Hund's coupling J_H is found to be sensitive to the Nd magnetic moment. The exchange coupling J in NdNiO₂ is only half as large as in the cuprates, which may explain why T_c in the nickelates is half as large as the cuprates.

Introduction

Since the discovery of high- T_c superconductivity (HTSC) in the lanthanum-based cuprates in 1986 [1], understanding the mechanism of HTSC has drawn intense interest [2–6]. Despite vigorous efforts, however, many unanswered questions still remain and a clear consensus on the underlying mechanism of HTSC has not been reached. A promising route in this connection is to find superconducting analogs of the cuprates which could provide new clues to the origin of HTSC. One such candidate materials is the perovskite nickel oxides. Specifically, the infinite-layer NdNiO₂ compound holds great promise since it exhibits an intrinsic $3d^9$ filling much like the cuprates, although challenges of crystal growth have presented problems for undertaking systematic investigations of this material.

Recently, superconductivity in the hole-doped infinite-layer nickelate NdNiO₂ at 9~15K has been reported in thin film samples grown on SrTiO₃ [7–10], although

superconductivity in bulk NdNiO₂ has not been observed [11]. These results [7] have reinvigorated interest in searching for the microscopic mechanism of HTSC and stimulated many new open questions [10–20]. Notably, superconductivity is present both in hole-doped NdNiO₂ [7] and PrNiO₂ [21], but absent in LaNiO₂ [7]. This suggests that the Nd (Pr) *f*-electrons are not merely spectators, but possibly participate in the emergence of superconductivity. Interestingly, initial reports showed metallic behavior in pristine LaNiO₂ and NdNiO₂ [8, 10] with no sign of long range magnetic order, persisting down to low temperatures [11, 22], calling into question the role of Mott physics in HTSC. However, two recent transport studies [8, 10] report the presence of a weak insulating phase in pristine NdNiO₂, which could in part be a signature of short-range magnetic fluctuations due to the intrinsic off-stoichiometry produced by the inhomogeneous oxygen deintercalation crystal-growth process [7].

In order to address these questions, a variety of theoretical studies have been performed, employing density functional theory (DFT) [14, 18, 23–25], ‘beyond’ DFT methods, such as DFT+ U [18, 26, 27], quasiparticle GW [28], dynamical mean-field theory (DMFT) [26, 29–31], and model Hamiltonians [15, 17, 26, 32] that have been constructed to understand the low-energy physics.

* rzhang16@tulane.edu

† ar.bansil@neu.edu

‡ jsun@tulane.edu

The bulk of these studies focus on the NiO₂ plane, finding differences in quantities such as the $d-p$ orbital splitting as compared to the cuprates [18] in accord with experimental reports [33]. However, by focusing on the NiO₂ plane neglects the effects of the f -electrons on the electronic and magnetic structure, despite the presence of superconductivity in Nd and Pr based compounds but not in La [7, 21]. The active role of the f -electrons is also suggested by a Kondo-like logarithmic temperature dependence of the resistivity and the Hall coefficient at low temperatures [7], and other recent experiments demonstrating strong similarities between the infinite-layer nickelates and rare earth intermetallics [33], although a recent study attributes this strange behavior to the Nd $5d$ orbitals [15]. A few electronic structure studies utilizing the DFT+U [16] and Heyd-Scuseria-Ernzerhof (HSE) hybrid functional [24] approaches have considered the f -electrons and find significant hybridization between the Nd $4f$ and Ni $3d$ orbitals near the chemical potential along with a possible ferromagnetic order. But, these calculations neglected the effect of spin-orbit coupling (SOC) crucial to capture the correct f -band splittings and required the introduction and fine tuning of external *ad hoc* parameters such as the Hubbard U and the exact-exchange admixture, which limit their predictive power [34].

In this article, we present a systematic study of the electronic and magnetic structures of both LaNiO₂ and NdNiO₂ using the strongly-constrained-appropriately-normed (SCAN) density functional [35] with spin-orbit coupling to examine effects of the f -electron physics. The SCAN functional has a proven track record of accurately modeling many correlated materials families including the cuprates [36–40], iridates [41], and ABO₃ materials [42]. In particular, SCAN accurately predicts the f -band splitting in SmB₆ in good accord with experimental values [43]. We consider several magnetic phases, whose energy and ordering are found to be quite similar for LaNiO₂ and NdNiO₂, reflecting their sensitivity to the opening of magnetic gaps in the Ni $d_{x^2-y^2}$ band. Dispersion of this band is quite similar to the corresponding band in cuprates, as is the order of the resulting magnetic phases, with an antiferromagnetic state having the lowest energy. In line with this, the estimated values of the Hubbard U are close to those commonly found in the cuprates, while Hund J_H varies for different Nd magnetic sublattice. In contrast, we find the the intralayer nearest-neighbor exchange coupling J approximately one half as large as that in La₂CuO₄ [36]. Lastly, the $4f$ -electrons play an important role in modifying the Fermi surfaces. We find the charge transfer energy between Ni $3d$ and O $2p$ orbitals is large and does not change much with magnetic order. These latter findings suggest distinct physics in nickelates, which could be confirmed by further experiments.

Results and Discussion

Crystal and magnetic structures: Figure 1 shows

the crystal structure of LaNiO₂ and NdNiO₂ in the $P4/mmm$ symmetry [22], where NiO₂ planes are sandwiched together with La or Nd spacer layers. In the NiO₂ planes the Ni sites are surrounded by four O atoms in square-planar coordination. While the non-magnetic (NM) and ferromagnetic (FM) phases can be calculated in the primitive cell [Figs. 1 (a) and 1 (b)], the remaining three antiferromagnetic (AFM) phases require distinct supercells. Specifically, we use a $\sqrt{2} \times \sqrt{2} \times 1$, $\sqrt{2} \times \sqrt{2} \times 2$, and $1 \times 1 \times 2$ supercell for the C -type AFM (C -AFM), G -type AFM (G -AFM), and A -type AFM (A -AFM) orders, respectively, as shown in Figs. 1 (c)-(e). In the C -AFM phase, the intralayer coupling in both Nd and Ni layers is AFM, whereas the interlayer is FM coupled. In the G -AFM phase both the intra- and interlayer coupling are AFM. In contrast, the A -AFM phase displays an intralayer FM coupling with an AFM interlayer coupling for both Nd and Ni sublattices. We note that the coupling between Ni and Nd nearest neighbors is frustrated in the A -AFM and G -AFM configurations.

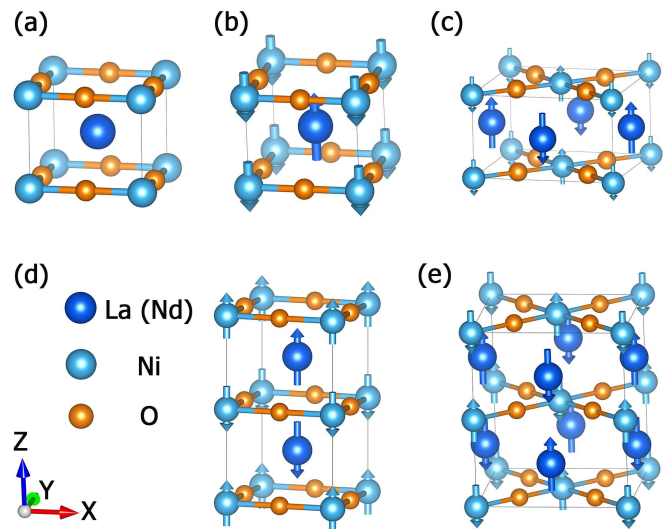


FIG. 1. (a) Non-magnetic (NM), (b) ferromagnetic (FM), (c) C -type antiferromagnetic (C -AFM), (d) A -type antiferromagnetic (A -AFM) and (e) G -type antiferromagnetic (G -AFM) phase. The blue, gray, and yellow balls represent La (Nd), Ni and O atoms, respectively. The blue and gray arrows denote different magnetic moment directions. Note that there is no local magnetic moment on La.

Table I gives our theoretically predicted total energies, lattice constants, and spin magnetic moments for various magnetic phases of LaNiO₂ and NdNiO₂. For LaNiO₂, the C -AFM phase is the most stable, with the G -AFM, A -AFM, and NM phases lying at higher energies. Upon optimizing the crystal structure we find the predicted lattice parameters for the magnetic phases in good accord with the experimental values, while those from the NM phase are quite further away. Moreover, the lattice constant and energy of the FM (C -AFM) phase are almost

same as in the A -AFM (G -AFM) phase, suggesting that interlayer coupling in LaNiO_2 is very weak. Finally, our theoretically predicted local nickel magnetic moment is $\sim 1.0 \mu_B$ irrespective of the magnetic configuration.

Our results are in contrast to those found with GGA+U [18, 44] ($U = 3$) which predict a much smaller energy separation between the magnetic configurations along with reduced magnetic moments of $\sim 0.7 \mu_B$ and $\sim 0.5 \mu_B$ in the C -AFM and FM phases, respectively. The reduced moment values could possibly be due to SOC effects being neglected, but this result is still surprising since a significant Hubbard U was introduced on the Ni sites.

TABLE I. Comparison of various theoretically predicted properties for different magnetic phases of LaNiO_2 and NdNiO_2 . The lattice constants are for the primitive cell, and the energies are relative to reference C -AFM phase. The magnetic moments in these phases have small variations in magnitude among the different sites of Nd and Ni, so the results given here are the average values. M_{Nd} and M_{Ni} represent the local magnetic moment per Nd and Ni atom, respectively.

LaNiO ₂						
Phases	Lattice Constant (Å)			Energy (meV/f.u.)	M_{Ni} (μ_B)	
	a	b	c			
NM	3.896	3.896	3.384	+404	0	
C -AFM	3.947	3.947	3.347	0	1.02	
G -AFM	3.947	3.947	3.345	+21	0.96	
FM	3.942	3.942	3.354	+62	0.98	
A -AFM	3.941	3.941	3.358	+60	1.00	
Exp. [45]	3.959	3.959	3.375	-	-	

NdNiO ₂						
Phases	Lattice Constant (Å)			Energy (meV/f.u.)	M_{Nd} (μ_B)	M_{Ni} (μ_B)
	a	b	c			
NM	3.866	3.866	3.222	+3840	0	0
C -AFM	3.910	3.910	3.239	0	2.91	1.04
G -AFM	3.911	3.911	3.239	+134	2.91	0.94
FM	3.874	3.874	3.298	+65	3.04	0.94
A -AFM	3.887	3.887	3.269	+141	2.95	0.94
Exp. [20]	3.914	3.914	3.239	-	-	-

We now compare our LaNiO_2 results to the corresponding properties of NdNiO_2 (see Table I). For both compounds the C -AFM configuration is the ground state, with almost the same energy separation with the FM phase. However, the energy differences between the other AFM phases are much larger in NdNiO_2 than those in LaNiO_2 , with the NM phase lying at 3840 meV/f.u. The larger energy differences in NdNiO_2 between the FM (G -AFM) and A -AFM (C -AFM) phases suggests that the

interlayer exchange coupling is strongly affected by the presence of the local magnetic moment of Nd. Furthermore, like LaNiO_2 , the lattice constants of NdNiO_2 in the C - and G -AFM phases are extremely close to the experimental values compared to those obtained in the NM, FM, and A -AFM arrangements. The stabilization of C -AFM order over that of G -AFM appears to be due to the frustration between Nd and Ni magnetic moments, clearly illustrating the importance of the Nd f -electrons in the calculation.

Table I shows the theoretically predicted local magnetic moments of Nd and Ni to be $\sim 3.0 \mu_B$ and $\sim 1.0 \mu_B$, respectively. This suggests that the electron configuration of Nd and Ni are $[\text{Xe}] 4f^3$ and $3d^9$, respectively. By breaking the Ni magnetic moment down into the various orbital contributions, we find $0.75 \mu_B$ and $0.25 \mu_B$ on the $d_{x^2-y^2}$ and d_{z^2} orbitals, respectively, where the t_{2g} states have negligible moments. A number of theoretical studies in the literature have reported magnetic ordering and the associated local moments [16, 27, 44, 46] with strong spin fluctuations possibly playing a key role in Cooper pairing [31, 46, 47]. Specifically, the GGA finds the local moment on Ni to be significantly reduced, yielding ~ 0.52 and $\sim 0.35 \mu_B$ in the FM and AFM phases, respectively [16]. Where the SCAN values are only recovered when a large Hubbard U of 8 (5) eV for Nd (Ni) is assumed [16]. Moreover, a previous calculation utilizing the SCAN functional [25] surprisingly finds reduced Ni magnetic moment values of $0.76 \mu_B$ [25], but these calculations neglect Nd $4f$ electrons and SOC effects. Lastly, the HSE06 hybrid functional finds stabilized moments of $\sim 3.03 \mu_B$ and $\sim 0.89 \mu_B$ on Nd and Ni sites, respectively, for the FM phase [24], similar to the SCAN values. Overall, the SCAN predictions are closely aligned with the expected d and f -filling of NdNiO_2 without any fine-tuning.

Electronic structure of NM Phase: Figures 2 (a) and 2 (b) show the theoretically obtained band structures and density of states (DOS) for LaNiO_2 and NdNiO_2 in the non-magnetic (NM) phase, with the various orbital-resolved atomic site projections overlaid. For LaNiO_2 , Fig. 2 (a), we find two distinct bands crossing the Fermi level: one of nearly pure Ni- $3d_{x^2-y^2}$ character, and the other composed of Ni ($3d_{z^2}$, $3d_{xy/yz}$) and La $5d$ orbitals. The latter band produces a 3D spherical electron-like Fermi surface at Γ and A [Fig. 2 (c)], whereas the former generates a large slightly warped quasi-2D cylindrical Fermi surface similar to the cuprates. These findings are consistent with previous LDA [18], GGA [24], DFT+U [44], and LDA+DMFT [30] studies. We note that the $3d_{x^2-y^2}$ band bears a striking resemblance to the corresponding band in cuprates [36], except for a shift of the VHS energy between Γ and Z planes in the Brillouin zone. The shifting of the VHS from below to above the Fermi level along k_z is directly reflected in the Fermi surface transitioning from being open to closed in the Γ and Z planes, respectively [Fig. 2 (c)].

On comparing LaNiO_2 with NdNiO_2 [Fig. 2 (b)], we

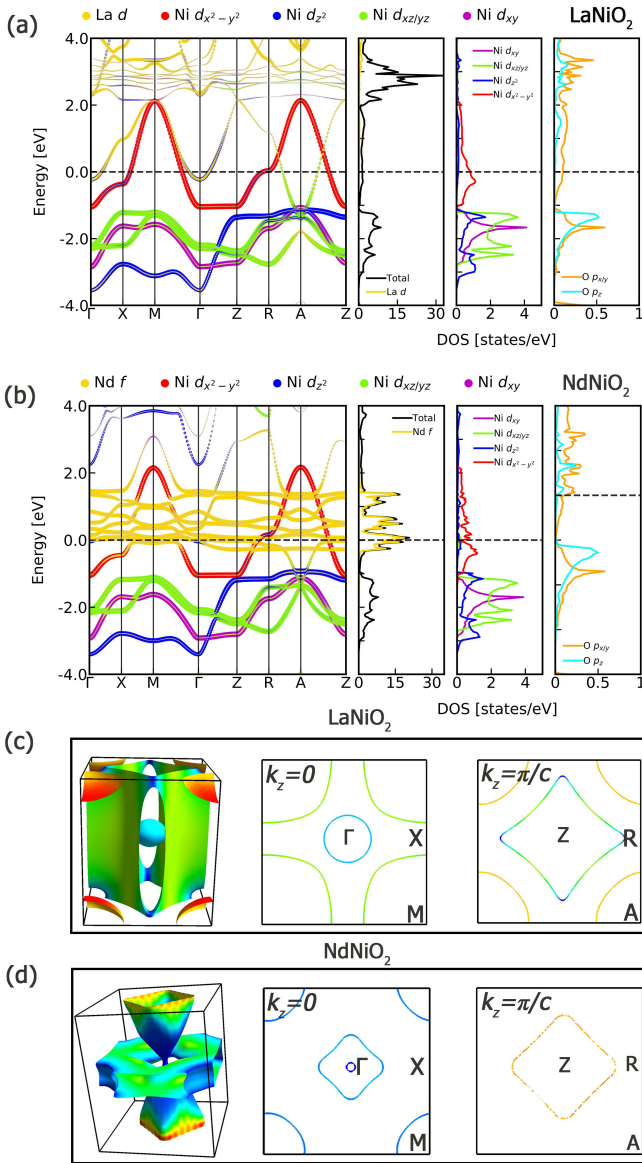


FIG. 2. Orbital projected electronic structures of NM (a) LaNiO₂ and (b) NdNiO₂. (c) The calculated Fermi surface of LaNiO₂ and the projection of Fermi surface on $k_z = 0$ and π/c plane. (d) Same as (c) but for NdNiO₂. Red, green, and blue indicate the maximum, middle, and minimum Fermi velocity, respectively.

find all the Ni bands to be relatively unchanged, except for significant hybridization between the Nd 4*f*-electrons and Ni 3*d*_{*x*²-*y*²} orbitals. Interestingly, this similarity between the Ni 3*d* dispersions in LaNiO₂ and NdNiO₂ persists across all magnetic phases studied [Figs. 3–6]. The significant hybridization between Ni 3*d* and Nd 4*f* levels can give rise to self-doping effects and induce Kondo physics [23, 25–27, 29]. Such hybridizations also radically alter the Fermi surfaces. Figure 2 (d) displays a double-goblet-like hole pocket along the Γ -*Z* direction, with a very narrow stem at Γ . Moreover, a large and complex

hole Fermi surface appears surrounding Γ near the $k_z = 0$ plane, along with the formation of electron pockets near *M*. We further note that the narrow neck of the goblet Fermi surface at Γ suggests that the system is close to a Fermi surface topological transition where the goblet splits into Fermi pockets centered on the *Z* point [Fig. 2 (d)].

Electronic structure of C-AFM Phase: Figures 3 (a) and 3 (b) present the unfolded theoretical electronic structure of LaNiO₂ and NdNiO₂ in the *C*-AFM phase. Similar to the cuprates, the *C*-AFM order is stabilized by opening a 2 eV band gap in the *d*_{*x*²-*y*²} dominated band. However, unlike the cuprates, 5*d* and 4*f* states fill the gap maintaining the metallic nature of these compounds. For example, the states near the Fermi level in LaNiO₂ are mainly governed by the Ni 3*d*_{*z*²} and La 5*d* orbitals [Fig. 3 (a)]. Moreover, an extremely flat band is found pinned near the Fermi level along the *Z*–*R*–*A*–*Z* line, originating from the La 5*d* and Ni 3*d*_{*z*²} hybridized orbitals. A similar flat band is found in NdNiO₂, along with a second flat band along *Z*–*R*–*A*, stemming from Nd 4*f*Ni 3*d*_{*x**y*}/*y**z* hybridization. These flat band features have also been observed by Choi et. al [46] where a large *U* was used to push the Nd 4*f* states away from the Fermi level. These flat-band features also produce highly anisotropic Fermi surfaces near the $k_z = \pi/c$ plane for both LaNiO₂ and NdNiO₂ [Fig. 3 (c) and (d)]. For NdNiO₂ there are two additional heavy electron pockets ellipsoidal in shape [Fig. 3(d)], which are induced by strong Nd 4*f* and Ni 3*d*_{*z*²} hybridization.

Electronic structure of G-AFM Phase: While the *C*-AFM phase is found to be the ground state, it is important to study other low-lying phases in correlated quantum materials that could contribute to various intertwined orders [36, 37, 41–43]. Figure 4 (a) and 4(b) show the electronic structures of LaNiO₂ and NdNiO₂ in the *G*-AFM phase. The *G*-AFM magnetic phase exhibits AFM coupling between the intra- and interlayer magnetic sites, in contrast to *C*-AFM where the interlayer coupling is FM. Interestingly, here we find no *f*-bands near the Fermi level for NdNiO₂, making the Fermi surfaces in LaNiO₂ and NdNiO₂ equivalent. While both *G*-AFM and *C*-AFM phases are dominated by the splitting of the *d*_{*x*²-*y*²}-band, and both have a region of suppressed DOS within ~ 0.7 eV of the Fermi level, they differ in that a 3*d*_{*z*²} band is above the low DOS region in the *C*-AFM phase, but below it in the *G*-AFM phase, causing the Fermi energy to shift by ~ 0.7 eV.

Electronic structure of FM Phase: Figures 5 (a) and 5 (b) present the electronic structure of LaNiO₂ and NdNiO₂ in the FM phase. Although the spin moments of Nd and Ni were initialized in the same direction, the system self-consists into a ferrimagnetic configuration [Fig. 1 (b)]. Compared with the NM phase [Fig. 2], the Ni 3*d*_{*x*²-*y*²} and 3*d*_{*z*²} bands are spin split, due to the spin-polarization in FM phase. In this case the Fermi surface is composed of a Ni 3*d*_{*x*²-*y*²} hole pocket (red) at the *M* point and an electron pocket from the hybridization

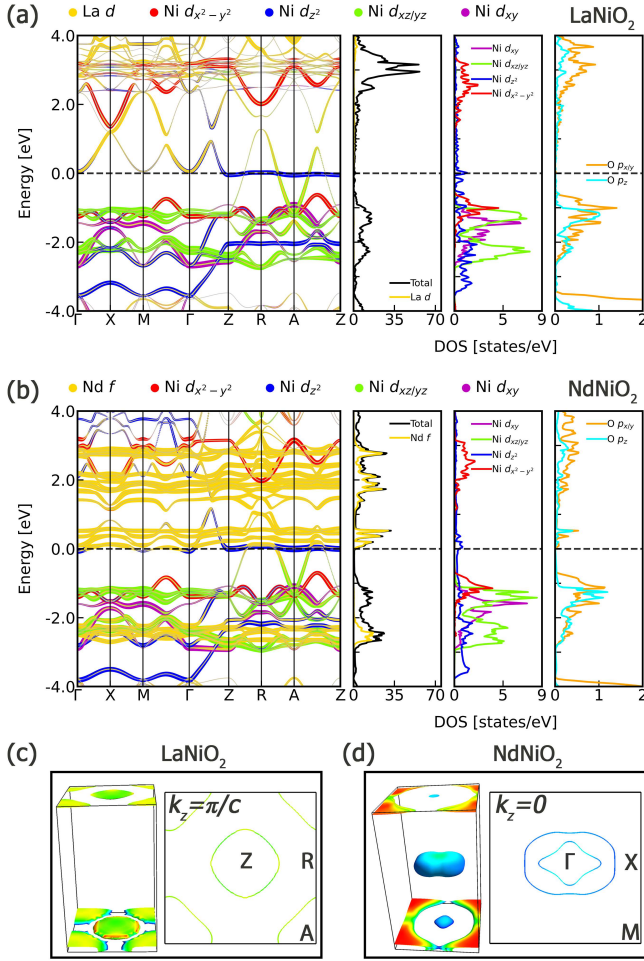


FIG. 3. Orbital projected electronic structures of C -AFM phase of (a) LaNiO_2 and (b) NdNiO_2 . The band structures are unfolded to the primitive $1 \times 1 \times 1$ BZ. (c) The calculated Fermi surface of LaNiO_2 and the projection of Fermi surface on $k_z = \pi/c$ plane. (d) Same as (c) but for NdNiO_2 . Red, green, and blue indicate the maximum, middle, and minimum Fermi velocity, respectively.

between Ni $3d_{z^2}$ and Nd $4f$ orbitals at Γ point (blue) [Fig. 5 (b)]. Interestingly, the majority spins in the Ni $3d_{x^2-y^2}$ and $3d_{z^2}$ bands point in opposite directions for a given atom. Figs. 5 (c) and (d) show that the Fermi surfaces of these two compounds are quite similar, except that the Γ point electron pocket in Fig. 5 (c) has grown ‘propellers’ in Fig. 5 (d), which is due to hybridization between Ni $3d_{z^2}$ and Nd $4f$ orbitals. We also find a 2D Fermi sheet centered at the M point extending in the k_z direction, produced by hybridization between the Ni $3d_{xy/yz}$ and Nd $4f$ orbitals. Finally, there is an A -centered hole pocket generated by the Ni $3d_{x^2-y^2}$ band.

Electronic structure of A-AFM Phase: Figures 6 (a) and 6 (b) display the unfolded electronic band structure and density of states of LaNiO_2 and NdNiO_2 in the A-AFM phase. Since the NiO_2 layers are ferromagneti-

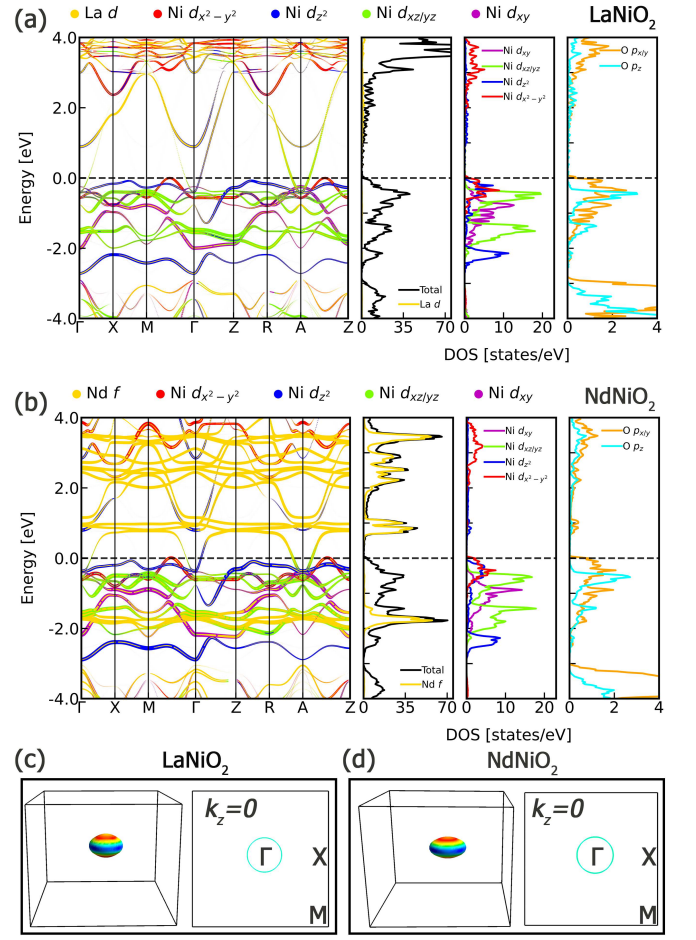


FIG. 4. Orbital projected electronic structures of G -AFM phase of (a) LaNiO_2 and (b) NdNiO_2 . The band structures are unfolded to the primitive $1 \times 1 \times 1$ BZ. (c) The calculated Fermi surface of LaNiO_2 and the projection of Fermi surface on $k_z = 0$ plane. (d) Same as (c) but for NdNiO_2 . Red, green, and blue indicate the maximum, middle, and minimum Fermi velocity, respectively.

cally ordered, the resulting band-splitting is quite similar to the FM phase [Fig. 5]. Figure 6 (a), shows that the bands near the Fermi level in LaNiO_2 are mainly of Ni $3d_{x^2-y^2}$, and hybridized Ni $3d_{z^2}$ and La $5d$ character. However, in NdNiO_2 , we find the main low-lying states near the Fermi level to originate from Nd $4f$ states hybridizing with Ni $3d_{x^2-y^2}$ and $3d_{z^2}$ orbitals. Notably, around -1 eV we see a strong mixing between the Ni $3d_{x^2-y^2}$ and $3d_{z^2}$ orbitals in both LaNiO_2 and NdNiO_2 along $\Gamma - X$ and $R - A$ directions, which are absent in the NM and FM phases. Such a strong ‘orbital-mixing’ effect could make the physics in the nickelates quite different from the cuprates.

From Figs. 6 (c) and 6 (d), the Fermi surfaces of LaNiO_2 and NdNiO_2 fall into two categories. (i) The $M - A$ direction in both materials is similar to the corresponding FM Fermi surfaces, except for the splitting

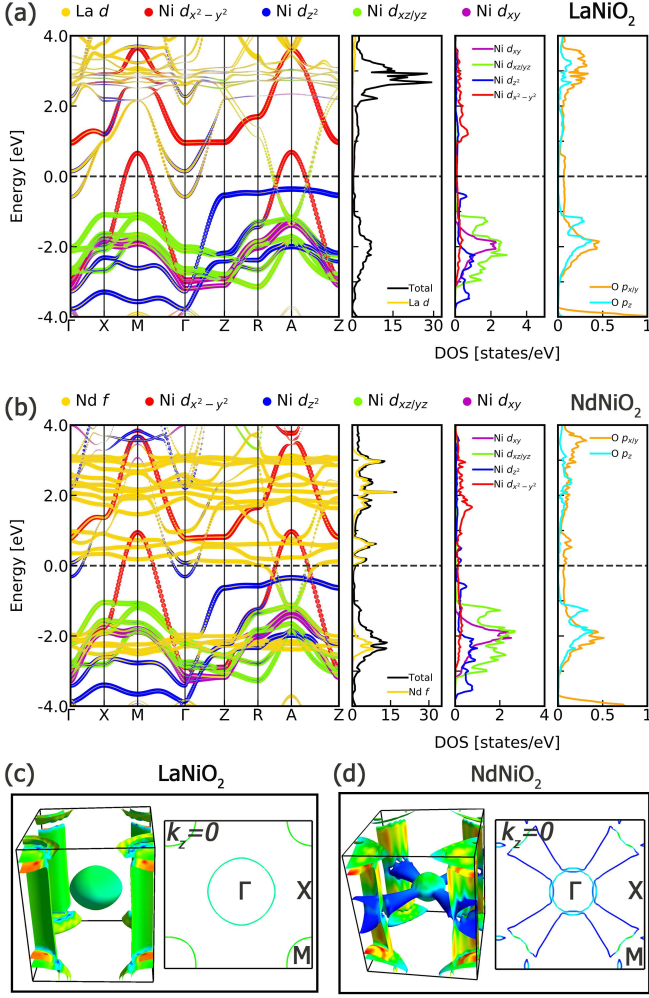


FIG. 5. Orbital projected electronic structures of FM phase of (a) LaNiO₂ and (b) NdNiO₂. (c) The calculated Fermi surface of LaNiO₂ and the projection of Fermi surface on $k_z = 0$ plane. (d) Same as (c) but for NdNiO₂. Red, green, and blue indicate the maximum, middle, and minimum Fermi velocity, respectively.

along the *z*-axis due to the AFM stacking of adjacent FM layers. This effect leads to the appearance of two pockets near the M point in Γ -plane. (ii) The $\Gamma - Z$ direction is more reminiscent of the NM case, with a Ni $3d_{z^2}$ electron pocket at the Γ point in LaNiO₂, while in NdNiO₂, the goblet Fermi surface of the NM phase has split into Z-centered pockets. The blue color of these features (low Fermi velocity) suggests strong *f*-electron mixing.

***f*-electron dispersions:** Based on the preceding comparison of LaNiO₂ and NdNiO₂, we find the stabilization of the various magnetic phases of NdNiO₂ to be mainly driven by Ni *d*-electrons, with the *f*-electrons playing only a minor role. In contrast, the Fermi surfaces are strongly affected by the Nd 4*f*-electrons, exhibiting strong mixing with Ni 3*d* orbitals. While the *f*-electrons

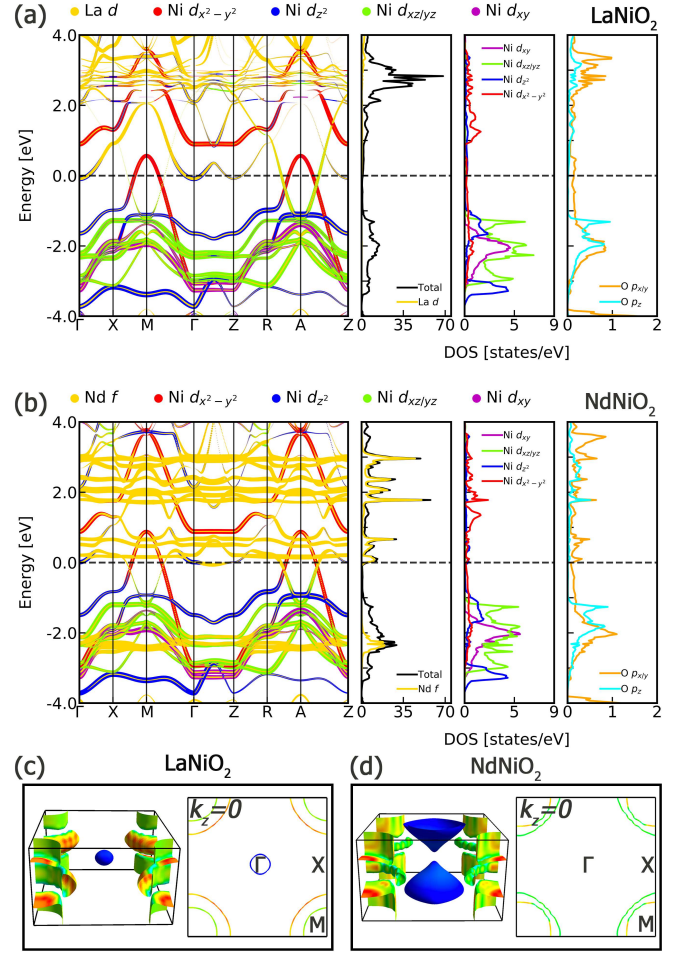


FIG. 6. Orbital projected electronic structures of A-AFM phase of (a) LaNiO₂ and (b) NdNiO₂. The band structures are unfolded to the primitive $1 \times 1 \times 1$ BZ. (c) The calculated Fermi surface of LaNiO₂ and the projection of Fermi surface on the $k_z = 0$ plane. (d) Same as (c) but for NdNiO₂. Red, green, and blue indicate the maximum, middle, and minimum Fermi velocity, respectively.

form one large cluster in the NM phase, they split into three subbands once the Nd atoms become polarized with slight shifts depending on the magnetic order consistent with our recent work on SmB₆ [43].

Comparisons with cuprates: Table II gives the calculated Δ_{dp} , Δ_{eg} , *U*, and *J_H* for the various magnetic phases of LaNiO₂ and NdNiO₂, along with the corresponding values for the cuprates for comparison. The values of Δ_{dp} for LaNiO₂ phases range from 1.58 (FM) to 2.08 eV (*G*-AFM), while the corresponding values for NdNiO₂ span 1.82 to 2.84 eV. To illustrate the charge-transfer gap further and compare to *C*-AFM of the infinite-layer cuprate CaCuO₂ the partial density of states for the Ni (Cu) 3*d* and O 2*p* orbitals is shown in Figs. 7 (a) and (c). Here, the O 2*p* band-center is clearly lower than the center of gravity of the Ni 3*d* states by

~ 2 eV in NdNiO₂, whereas the O 2*p* levels are strongly hybridized with Cu 3*d*_{*x*²-*y*²} orbitals near the Fermi level in CaCuO₂. To quantify this, we find Δ_{dp} for CaCuO₂ in the *C*-AFM phase to be 0.19 eV, which is significantly smaller than nickel-based compounds. Additionally, we estimated Δ_{dp} for the single-layer La₂CuO₄ in the *G*-AFM phase to be 0.6 eV, still much smaller than nickelates. Based on these results, LaNiO₂ and NdNiO₂ are closer to the Mott-Hubbard limit rather than charge-transfer case based on the ZaanenSawatzkyAllen classification scheme [48].

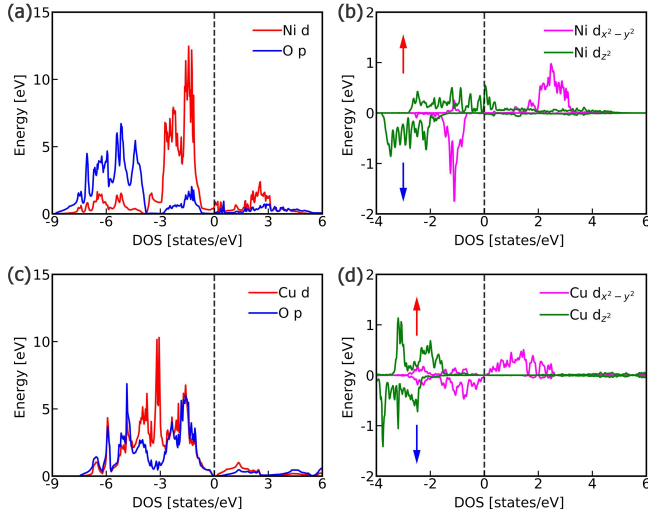


FIG. 7. (a) Partial densities of states in the *C*-AFM phase of NdNiO₂, where red and blue lines represent the Ni and O 2*p* orbitals, respectively. (b) Single nickel-site-resolved partial densities of states in the *C*-AFM phase of NdNiO₂, where the magenta and green lines represent the Ni 3*d*_{*x*²-*y*²} and 3*d*_{*z*²} orbitals, respectively. And, the red and blue arrows represent the spin up and spin down channels, respectively. (c) and (d) same as (a) and (b), except that these panels refer to the *C*-AFM phase of CaCuO₂.

Interestingly, values of Δ_{e_g} for the various magnetic phases of LaNiO₂ and NdNiO₂ are very close to 2 eV. For example, the Δ_{e_g} for LaNiO₂ in the NM phase is 1.93 eV. Our estimate of Δ_{e_g} is consistent with the value of 1.95 eV obtained in Ref. 18. The similarity of Δ_{e_g} values across the infinite-layer nickelates suggests that the Nd 4*f* electrons play a very limited role in splitting the Ni 3*d* levels. Additionally, we estimate the value of Δ_{e_g} for *C*-AFM CaCuO₂ and *G*-AFM La₂CuO₄ to be close to those obtained from the nickelates [Table II]. This information also can be read from Figs. 7 (b) and (d), where *e_g* orbitals are quite splitting for both *C*-AFM NdNiO₂ and CaCuO₂.

To gauge the strength of correlations on the nickel site we calculate the Hubbard *U* and Hund's coupling *J_H* for LaNiO₂ and NdNiO₂ in various magnetic arrangements according to Eq.(1)-(3). We find the on-site potential *U* for LaNiO₂ and NdNiO₂ to be almost the same and very

close to values obtained for CaCuO₂ and La₂CuO₄, suggesting strong electron interactions in nickelates. Note that these estimated *U* values are also consistent with recent works [23, 49]. The behavior of *J_H* is more subtle. In general, *J_H* for nickelates and cuprates are very similar, whereas *J_H*s for NdNiO₂ are larger in the *A*-AFM and *G*-AFM phases, suggesting that *J_H* is highly sensitive to the interlayer coupling.

TABLE II. Comparison of properties of different phases of nickelates and cuprates. Δ_{dp} and Δ_{e_g} represent the splitting of the metallic (Ni and Cu) 3*d* and O 2*p* bands, and the splitting of transition metal ions (Ni and Cu) *e_g* bands, respectively. *U* and *J_H* are on-site Hubbard potential and Hunds coupling, respectively.

LaNiO ₂				
Phases	Δ_{dp} (eV)	Δ_{e_g} (eV)	<i>U</i> (eV)	<i>J_H</i> (eV)
NM	1.91	1.93	–	–
FM	1.58	2.23	4.88	1.01
<i>A</i> -AFM	1.57	1.93	4.99	1.14
<i>C</i> -AFM	1.68	2.02	5.21	1.11
<i>G</i> -AFM	2.08	2.09	5.70	1.45
NdNiO ₂				
Phases	Δ_{dp}	Δ_{e_g}	<i>U</i> (eV)	<i>J_H</i> (eV)
NM	2.84	1.94	–	–
FM	1.82	2.04	5.08	1.23
<i>A</i> -AFM	1.80	2.00	4.99	2.14
<i>C</i> -AFM	2.59	2.11	5.27	1.00
<i>G</i> -AFM	2.25	2.13	5.78	1.94
CaCuO ₂				
Phases	Δ_{dp}	Δ_{e_g}	<i>U</i> (eV)	<i>J_H</i> (eV)
<i>C</i> -AFM	0.19	2.65	5.35	1.29
La ₂ CuO ₄				
Phases	Δ_{dp}	Δ_{e_g}	<i>U</i> (eV)	<i>J_H</i> (eV)
<i>G</i> -AFM	0.6	1.23	4.85 [36]	1.25 [36]

Despite there being no clear theoretical description of the mechanism of HTSC, the view that spin-fluctuations play a central role in determining the physical properties of the cuprates has been gaining increasing support. Furthermore, in this picture, the exchange coupling strength is a good descriptor of the robustness of superconductivity.

In order to determine the strength of the exchange coupling, we map the total energies of the AFM and FM phases onto those of the nearest-neighbor spin-1/2 Heisenberg Hamiltonian in the mean-field approximation [36, 50]. The Heisenberg Hamiltonian gives a reason-

able description of the low-lying excitations for La_2CuO_4 , and thus a good estimate of the Heisenberg exchange parameter J [51], and we expect this also to be the case for the infinite-layer nickelates. In the mean-field limit, the difference in total energies of the FM and AFM phases is

$$\Delta E = E_{AFM} - E_{FM} = JNZS^2 \quad (1)$$

where N is the total number of magnetic moments, S is the spin on each site, and Z is the coordination number. Since the in-plane interactions within the Ni-O planes in $\text{La}(\text{Nd})\text{NiO}_2$ are much stronger than the interplanar interactions, we can take $Z = 4$. Since we normalize to one formula unit, $N = 1$. Using the total energies for the FM and C -AFM states obtained from our first-principles computations we find J to be 62 and 65 meV for LaNiO_2 and NdNiO_2 , respectively. These exchange parameters are half as large as those in La_2CuO_4 [36] and larger than those estimated in Ref. [17]. The small J is consistent with the finding that the AFM gap is twice as large as in cuprates, which in turn may be related to the larger value of Ni magnetic moments, which may be related to smaller Ni- d and O- p hybridization (larger Δ_{dp}).

TABLE III. Comparison of the intralayer exchange coupling between the two nearest Ni or Cu atoms for LaNiO_2 , NdNiO_2 , and La_2CuO_4 .

	LaNiO_2	NdNiO_2	La_2CuO_4
J (meV)	62	65	138 [36]

Superconductivity in the cuprates evolves out of a Mott insulator [3], whereas in the iron pnictides superconductivity emerges out of a metallic state [52] with strong local magnetic fluctuations. Is magnetic order necessary for d -electron high- T_c superconductivity? The new Ni-based superconductors appear to be a counterexample. However, both Ni and Nd sites typically display significant magnetic moments with considerable evidence of magnetic fluctuations or short-range order [31, 46]. Moreover, the undoped nickelates are not ordinary metals, but weak insulators [8, 10]. In our previous SCAN-based studies of other correlated materials, we found many low-energy magnetic phases indicative of prominent magnetic fluctuations [36, 37, 43]. In the nickelates, our study of the various AFM orders finds ~ 0.7 eV pseudogap (regions of low DOS) near the Fermi level, which could explain the weak insulating behavior. In Figure 8, we compare the AFM gaps in the ground state structures of the cuprates (a) and the nickelates (b). We find the gap is about twice as large in the nickelates as compared to the cuprates [36], which may explain why J is only half as large in the former.

Hence, we find great similarity between the cuprates and nickelates, both in the dispersion of the NM $d_{x^2-y^2}$

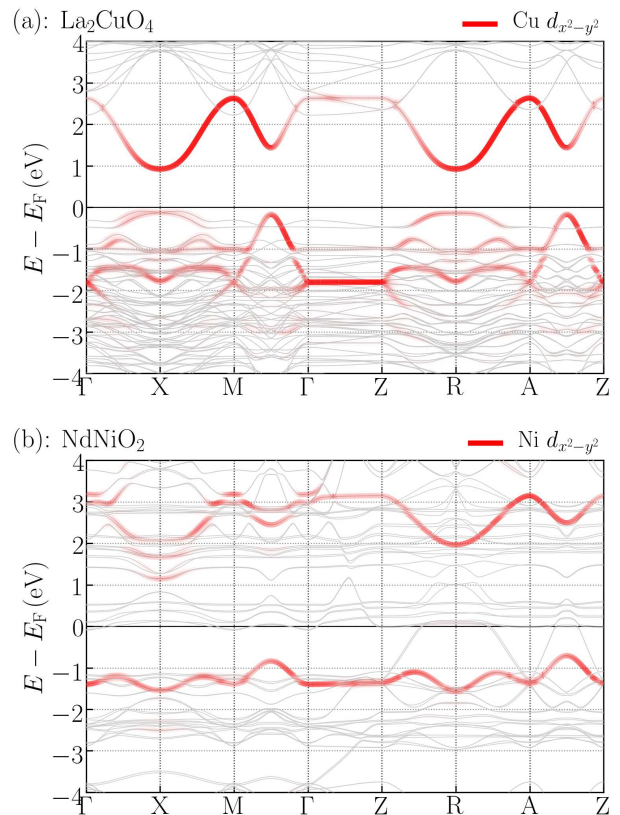


FIG. 8. (a) Cu $3d_{x^2-y^2}$ band for G -AFM La_2CuO_4 . (b) Ni $3d_{x^2-y^2}$ band for C -AFM NdNiO_2 . Band structures have been unfolded into the $1 \times 1 \times 1$ primitive BZ.

band, and in the resulting magnetic orders, with the f -electrons playing little role in the magnetic transitions despite significantly modifying the Fermi surfaces. In principle, the fact that J is only half as large in nickelates as in cuprates could tell us something about why the T_c dome is only half as large in nickelates. On the other hand, so far superconductivity has been found in two rare-earth substituted nickelates [7, 21], but not the parent La-based compound, suggesting a more significant role for f -electrons. An interesting possibility is that the f -electrons could lead to heavy-fermion physics (flat bands) not present in cuprates.

Conclusion: We examine in-depth the role of f -electrons and magnetic ordering effects in LaNiO_2 and NdNiO_2 within a parameter-free, all-electron first-principles framework. The magnetic orders in the nickelates are found to be very similar to those in the cuprates in that the transitions are driven by the gapping of the $d_{x^2-y^2}$ band. We find a reduced J value in the nickelate compared to the cuprates, however, which could explain the weaker superconductivity in the nickelates. While the $4f$ electrons play little role in the nickelate magnetism, they substantially modify Fermi surfaces for various mag-

netic states. Our study further reveals the importance of fluctuating magnetic order in correlated materials [37].

Methods

All calculations were performed by using the pseudopotential projector-augmented wave method [53] as implemented in the Vienna *ab initio* simulation package (VASP) [54, 55]. A high-energy cutoff of 520 eV was used to truncate the plane-wave basis set. The exchange-correlation effects were treated using the SCAN [35] meta-GGA scheme. Spin-orbit coupling effects were included self-consistently. The crystal structures and ionic positions were fully optimized with a force convergence criterion of 0.01 eV/Å for each atom along with a total energy tolerance of 10^{-5} eV. The Fermi surface was obtained with the FermiSurfer code [56]. The unfolded band structures including orbital characters are extracted from the supercell pseudo-wavefunction calculation [57], which has been implemented based on the VaspBandUnfolding code [58].

To facilitate comparison with the cuprates, we calculated two quantities: (1) charge-transfer energies between the Ni $3d$ and O $2p$ orbitals $\Delta_{dp} = \varepsilon_d - \varepsilon_p$ and (2) the energy splitting of the two Ni e_g orbitals $\Delta_{e_g} = \varepsilon_{x^2-y^2} - \varepsilon_{z^2}$. Here, ε_i refers to the band centers of the corresponding orbital i . Following previous works, [18, 59] the band

centers are defined as $\varepsilon_i = \frac{\int g_i(\varepsilon)\varepsilon d\varepsilon}{\int g_i(\varepsilon)d\varepsilon}$, where $g_i(\varepsilon)$ refers to the partial-density-of-states (PDOS) associated with orbital i . The integration range for Δ_{dp} is set to cover the full bonding and antibonding bands [59], whereas Δ_{e_g} is obtained from an integral over the antibonding bands alone, using an energy window of -3.5 to 2 eV and -4 to 4 eV for the NM and magnetic phases, respectively.

To estimate the on-site Hubbard potential U and the Hunds coupling J_H , we follow the method developed by Lane *et al.* [36]. Using the site-projected orbital-resolved partial DOS $g_{\mu\sigma}$, we determine the average spin-splitting of the μ levels as follows:

$$\bar{E}_{\mu\sigma} = \int_W E g_{\mu\sigma}(E) dE, \quad (2)$$

$$\bar{E}_{d_{x^2-y^2}\uparrow} - \bar{E}_{d_{x^2-y^2}\downarrow} = U(N_\uparrow - N_\downarrow), \quad (3)$$

$$\bar{E}_{\mu \neq d_{x^2-y^2}\uparrow} - \bar{E}_{\mu \neq d_{x^2-y^2}\downarrow} = J_H(N_\uparrow - N_\downarrow), \quad (4)$$

where N_\uparrow (N_\downarrow) is the occupation of the spin-up (down) $d_{x^2-y^2}$ orbital and the integration is over the full bandwidth W .

Data availability

The data that support the findings of this study are available from the corresponding author upon reasonable request.

-
- [1] J. G. Bednorz and K. A. Müller, *Z. Physik B - Condensed Matter* **64**, 189 (1986).
- [2] P. W. Anderson, *Science* **316**, 1705 (2007).
- [3] P. A. Lee, N. Nagaosa, and X.-G. Wen, *Reviews of Modern Physics* **78**, 17 (2006).
- [4] P. W. Anderson, P. A. Lee, M. Randeria, T. M. Rice, N. Trivedi, and F. C. Zhang, *Journal of Physics: Condensed Matter* **16**, R755 (2004).
- [5] M. R. Norman, *Science* **332**, 196 (2011).
- [6] B. Keimer, S. A. Kivelson, M. R. Norman, S. Uchida, and J. Zaanen, *Nature* **518**, 179 (2015).
- [7] D. Li, K. Lee, B. Y. Wang, M. Osada, S. Crossley, H. R. Lee, Y. Cui, Y. Hikita, and H. Y. Hwang, *Nature* **572**, 624 (2019).
- [8] S. Zeng, C. S. Tang, X. Yin, C. Li, Z. Huang, J. Hu, W. Liu, G. J. Omar, H. Jani, Z. S. Lim, K. Han, D. Wan, P. Yang, A. T. S. Wee, and A. Ariando, [arXiv:2004.11281](https://arxiv.org/abs/2004.11281).
- [9] Q. Gu, Y. Li, S. Wan, H. Li, W. Guo, H. Yang, Q. Li, X. Zhu, X. Pan, Y. Nie, and H.-H. Wen, [arXiv:2006.13123](https://arxiv.org/abs/2006.13123).
- [10] D. Li, B. Y. Wang, K. Lee, S. P. Harvey, M. Osada, B. H. Goodge, L. F. Kourkoutis, and H. Y. Hwang, *Physical Review Letters* **125**, 027001 (2020).
- [11] B.-X. Wang, H. Zheng, E. Krivyakina, O. Chmaissem, P. P. Lopes, J. W. Lynn, L. C. Gallington, Y. Ren, S. Rosenkranz, J. F. Mitchell, and D. Phelan, [arXiv:2006.09548](https://arxiv.org/abs/2006.09548).
- [12] G. A. Sawatzky, *Nature* **572**, 592 (2019).
- [13] M. R. Norman, *Physics* **13**, 85 (2020).
- [14] X. Wu, D. Di Sante, T. Schwemmer, W. Hanke, H. Y. Hwang, S. Raghu, and R. Thomale, *Physical Review B* **101**, 060504 (2020).
- [15] G.-M. Zhang, Y.-f. Yang, and F.-C. Zhang, *Physical Review B* **101**, 020501 (2020).
- [16] M. Y. Choi, K. W. Lee, and W. E. Pickett, *Physical Review B* **101**, 20503 (2020).
- [17] M. Jiang, M. Berciu, and G. A. Sawatzky, *Physical Review Letters* **124**, 207004 (2020).
- [18] A. S. Botana and M. R. Norman, *Physical Review X* **10**, 011024 (2020).
- [19] J. Karp, A. S. Botana, M. R. Norman, H. Park, M. Zingl, and A. Millis, *Physical Review X*, 021061.
- [20] Q. Li, C. He, J. Si, X. Zhu, Y. Zhang, and H.-H. Wen, *Communications Materials* **1**, 16 (2020).
- [21] M. Osada, B. Y. Wang, B. H. Goodge, K. Lee, H. Yoon, K. Sakuma, D. Li, M. Miura, L. F. Kourkoutis, and H. Y. Hwang, *Nano Letters* **20**, 57355740 (2020).
- [22] M. Hayward and M. Rosseinsky, *Solid State Sciences* **5**, 839 (2003).
- [23] Y. Nomura, M. Hirayama, T. Tadano, Y. Yoshimoto, K. Nakamura, and R. Arita, *Physical Review B* **100**, 205138 (2019).
- [24] P. Jiang, L. Si, Z. Liao, and Z. Zhong, *Physical Review B* **100**, 201106 (2019).
- [25] H. Zhang, L. Jin, S. Wang, B. Xi, X. Shi, F. Ye, and J.-W. Mei, *Physical Review Research* **2**, 013214 (2020).
- [26] Y. Gu, S. Zhu, X. Wang, J. Hu, and H. Chen, *Comm-*

- nications *Physics* **3**, 84 (2020).
- [27] Z. Liu, Z. Ren, W. Zhu, Z. Wang, and J. Yang, *npj Quantum Materials* **5**, 31 (2020).
- [28] V. Olevano, F. Bernardini, X. Blase, and A. Cano, *Physical Review B*, 161102.
- [29] F. Lechermann, *Physical Review B* **101**, 081110 (2020).
- [30] S. Ryee, H. Yoon, T. J. Kim, M. Y. Jeong, and M. J. Han, *Physical Review B* **101**, 064513 (2020).
- [31] I. Leonov, S. L. Skornyakov, and S. Y. Savrasov, *Physical Review B* **101**, 241108 (2020).
- [32] L.-H. Hu and C. Wu, *Physical Review Research* **1**, 1 (2019).
- [33] M. Hepting, D. Li, C. J. Jia, H. Lu, E. Paris, Y. Tseng, X. Feng, M. Osada, E. Been, Y. Hikita, Y.-D. Chuang, Z. Hussain, K. J. Zhou, A. Nag, M. Garcia-Fernandez, M. Rossi, H. Y. Huang, D. J. Huang, Z. X. Shen, T. Schmitt, H. Y. Hwang, B. Moritz, J. Zaanen, T. P. Devereaux, and W. S. Lee, *Nature Materials* **19**, 381 (2020).
- [34] K. Pokharel, C. Lane, J. W. Furness, R. Zhang, J. Ning, B. Barbiellini, R. S. Markiewicz, Y. Zhang, A. Bansil, and J. Sun, [arXiv:2004.08047](https://arxiv.org/abs/2004.08047).
- [35] J. Sun, A. Ruzsinszky, and J. Perdew, *Physical Review Letters* **115**, 036402 (2015).
- [36] C. Lane, J. W. Furness, I. G. Buda, Y. Zhang, R. S. Markiewicz, B. Barbiellini, J. Sun, and A. Bansil, *Physical Review B* **98**, 125140 (2018).
- [37] Y. Zhang, C. Lane, J. W. Furness, B. Barbiellini, J. P. Perdew, R. S. Markiewicz, A. Bansil, and J. Sun, *Proceedings of the National Academy of Sciences* **117**, 68 (2020).
- [38] J. W. Furness, Y. Zhang, C. Lane, I. G. Buda, B. Barbiellini, R. S. Markiewicz, A. Bansil, and J. Sun, *Communications Physics* **1**, 11 (2018).
- [39] J. Nokelainen, C. Lane, R. S. Markiewicz, B. Barbiellini, A. Pulkkinen, B. Singh, J. Sun, K. Pussi, and A. Bansil, *Physical Review B* **101**, 1 (2020).
- [40] C. Lane and J. X. Zhu, *Physical Review B* **101**, 1 (2020), 2003.00098.
- [41] C. Lane, Y. Zhang, J. W. Furness, R. S. Markiewicz, B. Barbiellini, J. Sun, and A. Bansil, *Physical Review B* **101**, 155110 (2020).
- [42] J. Varignon, M. Bibes, and A. Zunger, *Physical Review B* **100**, 035119 (2019).
- [43] R. Zhang, B. Singh, C. Lane, J. Kidd, Y. Zhang, B. Barbiellini, R. S. Markiewicz, A. Bansil, and J. Sun, (2020), [arXiv:2003.11052](https://arxiv.org/abs/2003.11052).
- [44] K. W. Lee and W. E. Pickett, *Physical Review B* **70**, 1 (2004).
- [45] D. Kaneko, K. Yamagishi, A. Tsukada, T. Manabe, and M. Naito, *Physica C: Superconductivity* **469**, 936 (2009).
- [46] M.-Y. Choi, W. E. Pickett, and K. W. Lee, [arXiv:2005.03234](https://arxiv.org/abs/2005.03234).
- [47] J. Chang, J. Zhao, and Y. Ding, [arXiv:1911.12731](https://arxiv.org/abs/1911.12731).
- [48] J. Zaanen, G. A. Sawatzky, and J. W. Allen, *Physical Review Letters* **55**, 418 (1985).
- [49] H. Sakakibara, H. Usui, K. Suzuki, T. Kotani, H. Aoki, and K. Kuroki, *Physical Review Letters*, 077003.
- [50] Y.-S. Su, T. Kaplan, S. Mahanti, and J. Harrison, *Physical Review B* **59**, 10521 (1999).
- [51] M. A. Kastner, R. J. Birgeneau, G. Shirane, and Y. Endoh, *Reviews of Modern Physics* **70**, 897 (1998).
- [52] M. Norman, *Physics* **1**, 21 (2008).
- [53] G. Kresse and D. Joubert, *Physical Review B* **59**, 1758 (1999).
- [54] G. Kresse and J. Hafner, *Physical Review B* **48**, 13115 (1993).
- [55] G. Kresse and J. Furthmüller, *Physical Review B* **54**, 11169 (1996).
- [56] M. Kawamura, *Computer Physics Communications* **239**, 197 (2019).
- [57] V. Popescu and A. Zunger, *Physical Review B* **85**, 085201 (2012).
- [58] Q. Zheng, “VaspBandUnfolding,” <https://github.com/QijingZheng/VaspBandUnfolding>.
- [59] S. W. Jang, T. Kotani, H. Kino, K. Kuroki, and M. J. Han, *Scientific Reports* **5**, 12050 (2015).

Acknowledgements

The work at Tulane University was supported by the start-up funding from Tulane University, the Cypress Computational Cluster at Tulane, the Extreme Science and Engineering Discovery Environment (XSEDE), the DOE Energy Frontier Research Centers (development and applications of density functional theory): Center for the Computational Design of Functional Layered Materials (DE-SC0012575), the DOE, Office of Science, Basic Energy Sciences Grant DE-SC0019350, and the National Energy Research Scientific Computing Center. The work at Northeastern University was supported by the U.S. DOE, Office of Science, Basic Energy Sciences grant number DE-FG02-07ER46352 (core research) and benefited from Northeastern Universitys Advanced Scientific Computation Center, the National Energy Research Scientific Computing Center supercomputing center (DOE grant number DEAC02-05CH11231), and support (testing the efficacy of new functionals in diversely bonded materials) from the DOE Energy Frontier Research Centers: Center for the Computational Design of Functional Layered Materials (DE-SC0012575). The work at Los Alamos National Laboratory was supported by the U.S. DOE NNSA under Contract No. 89233218CNA000001 and by the Center for Integrated Nanotechnologies, a DOE BES user facility, in partnership with the LANL Institutional Computing Program for computational resources. Additional support was provided by DOE Office of Basic Energy Sciences Program E3B5.

Author contributions

R.Z., C.L., B. S. and J. N. performed computations and analyzed the data. B.B., R.S.M., A.B. and J.S. led the investigations, designed the computational approaches, provided computational infrastructure and analyzed the results. All authors contributed to the writing of the manuscript.

Additional information

Competing interests: The authors declare no competing interests.

Figures

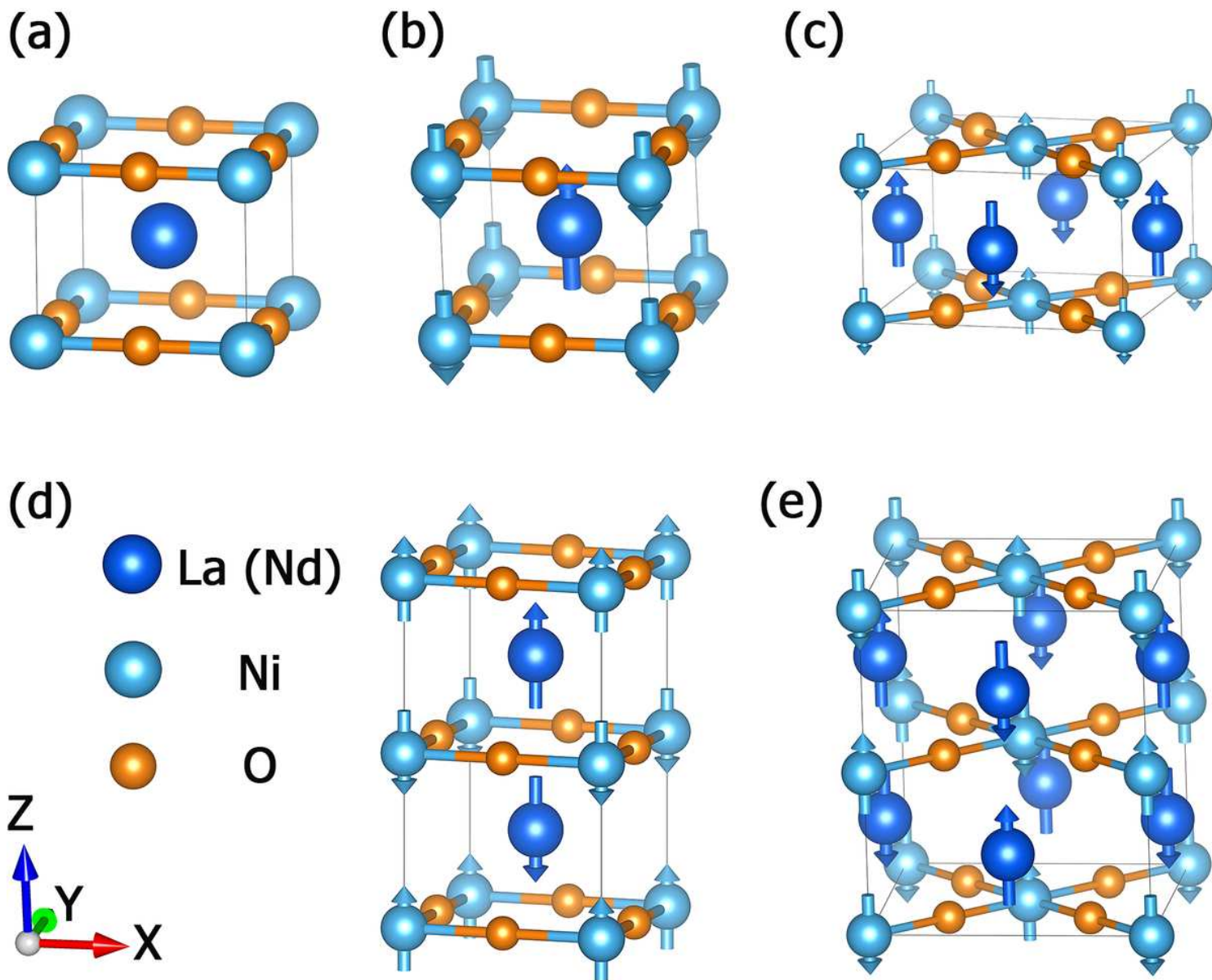


Figure 1

(a) Non-magnetic (NM), (b) ferromagnetic (FM), (c) C-type antiferromagnetic (C-AFM), (d) A-type antiferromagnetic (A-AFM) and (e) G-type antiferromagnetic (G-AFM) phase. The blue, gray, and yellow balls represent La (Nd), Ni and O atoms, respectively. The blue and gray arrows denote different magnetic moment directions. Note that there is no local magnetic moment on La.

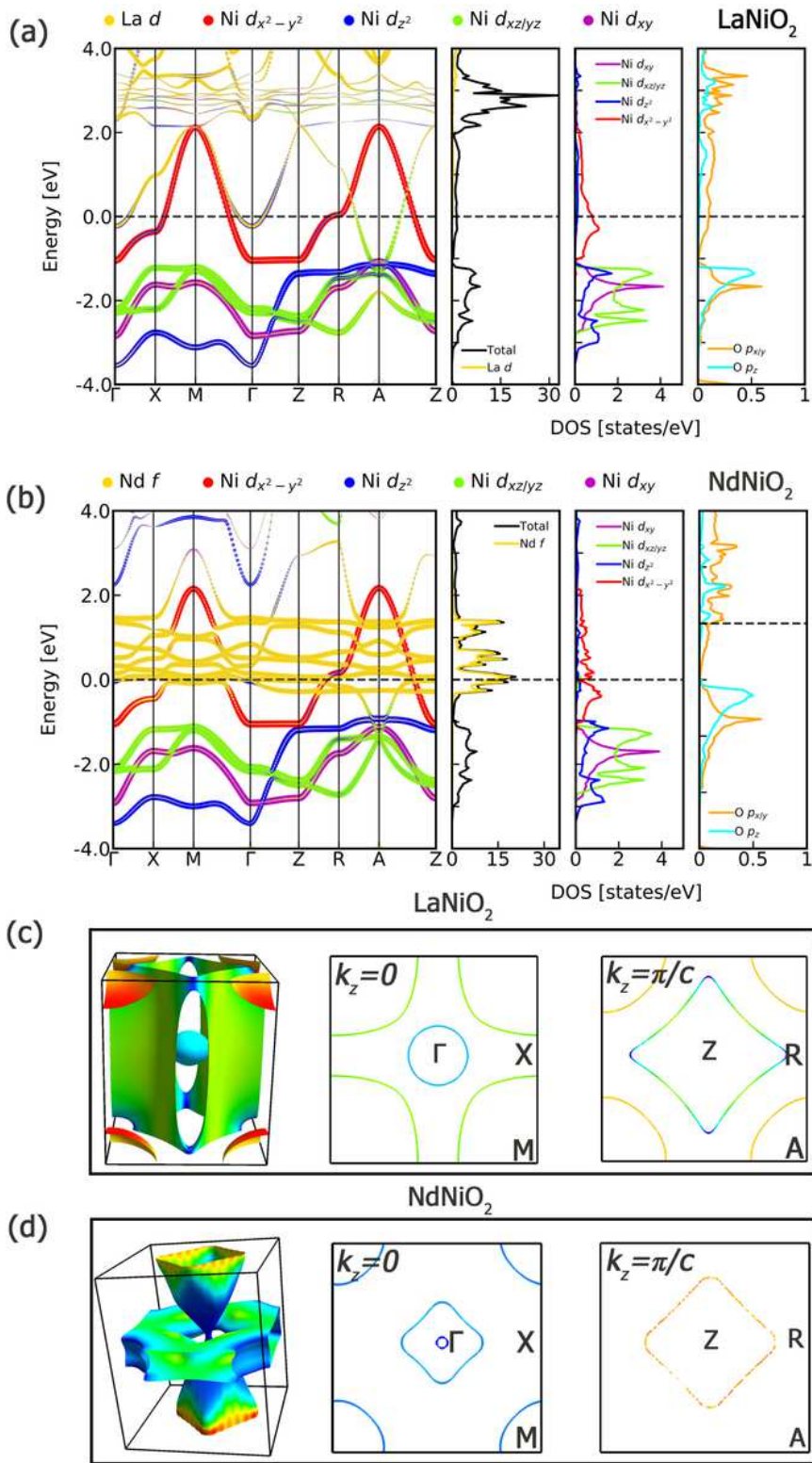


Figure 2

Orbital projected electronic structures of NM (a) LaNiO₂ and (b) NdNiO₂. (c) The calculated Fermi surface of LaNiO₂ and the projection of Fermi surface on $k_z = 0$ and $k_z = \pi/c$ plane. (d) Same as (c) but for NdNiO₂. Red, green, and blue indicate the maximum, middle, and minimum Fermi velocity, respectively.

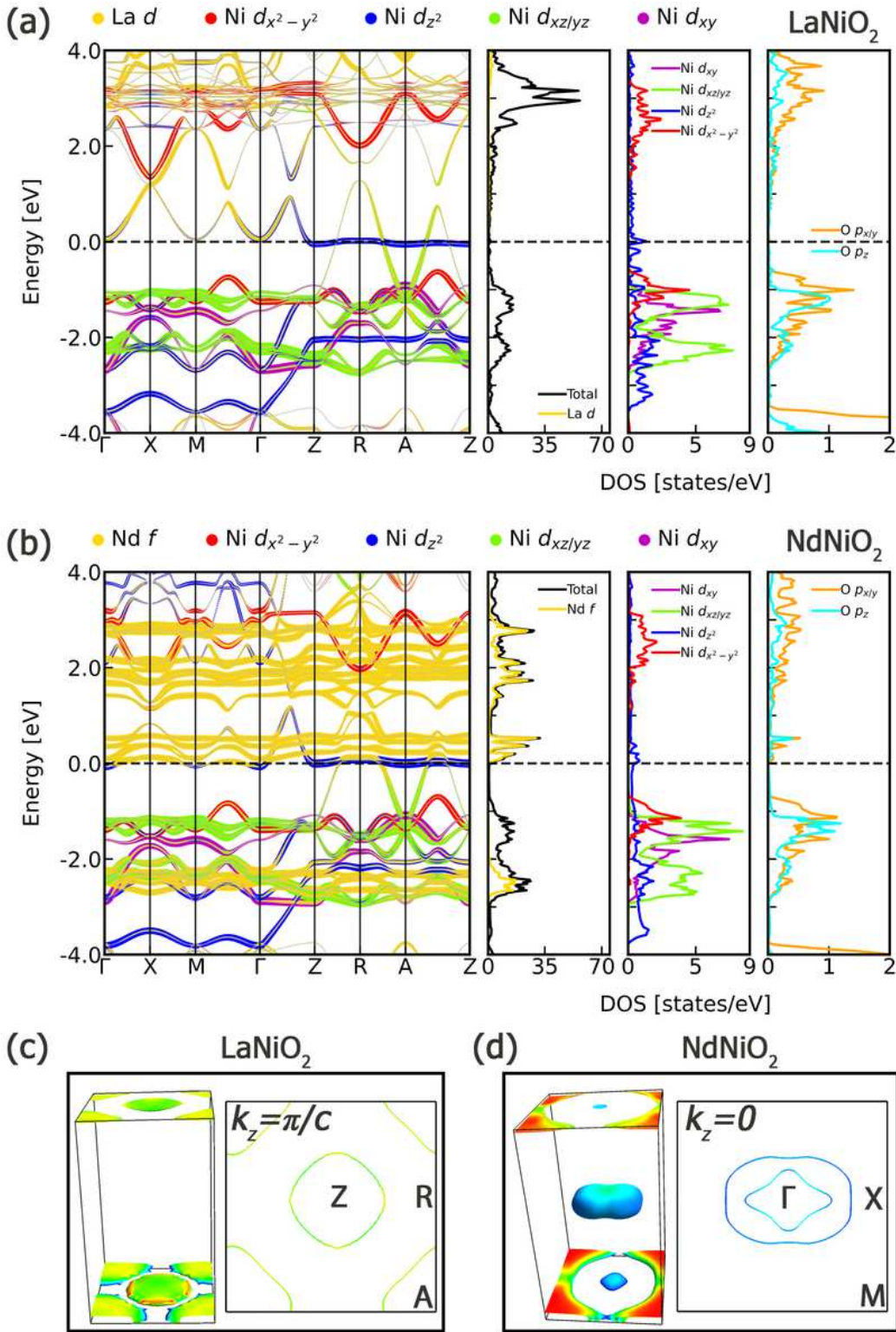


Figure 3

Orbital projected electronic structures of C-AFM phase of (a) LaNiO₂ and (b) NdNiO₂. The band structures are unfolded to the primitive $1 \times 1 \times 1$ BZ. (c) The calculated Fermi surface of LaNiO₂ and the projection of Fermi surface on $k_z = \pi/c$ plane. (d) Same as (c) but for NdNiO₂. Red, green, and blue indicate the maximum, middle, and minimum Fermi velocity, respectively.

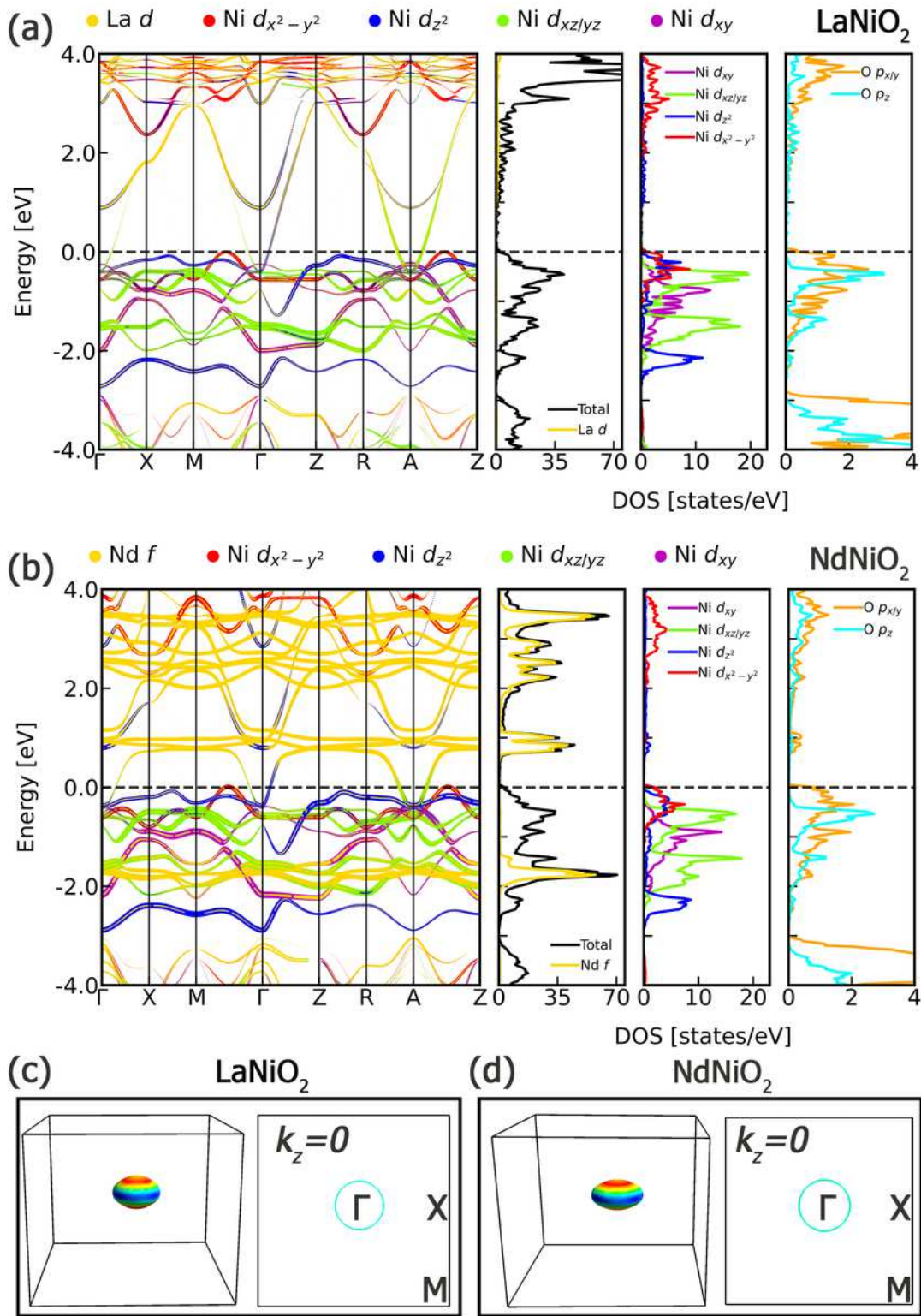


Figure 4

Orbital projected electronic structures of G-AFM phase of (a) LaNiO₂ and (b) NdNiO₂. The band structures are unfolded to the primitive 1 × 1 × 1 BZ. (c) The calculated Fermi surface of LaNiO₂ and the projection of Fermi surface on $k_z = 0$ plane. (d) Same as (c) but for NdNiO₂. Red, green, and blue indicate the maximum, middle, and minimum Fermi velocity, respectively.

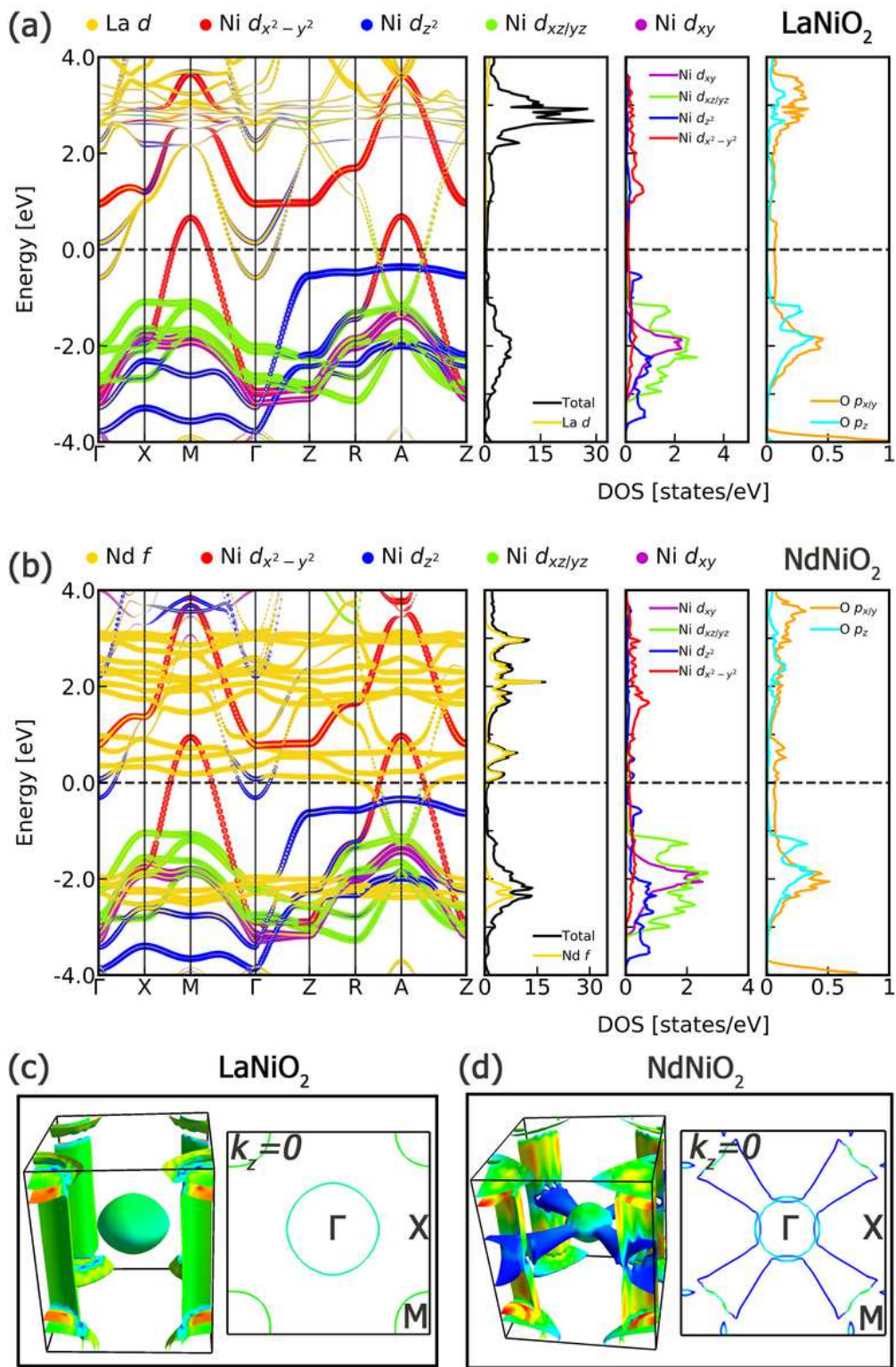


Figure 5

Orbital projected electronic structures of FM phase of (a) LaNiO₂ and (b) NdNiO₂. (c) The calculated Fermi surface of LaNiO₂ and the projection of Fermi surface on $k_z = 0$ plane. (d) Same as (c) but for NdNiO₂. Red, green, and blue indicate the maximum, middle, and minimum Fermi velocity, respectively.

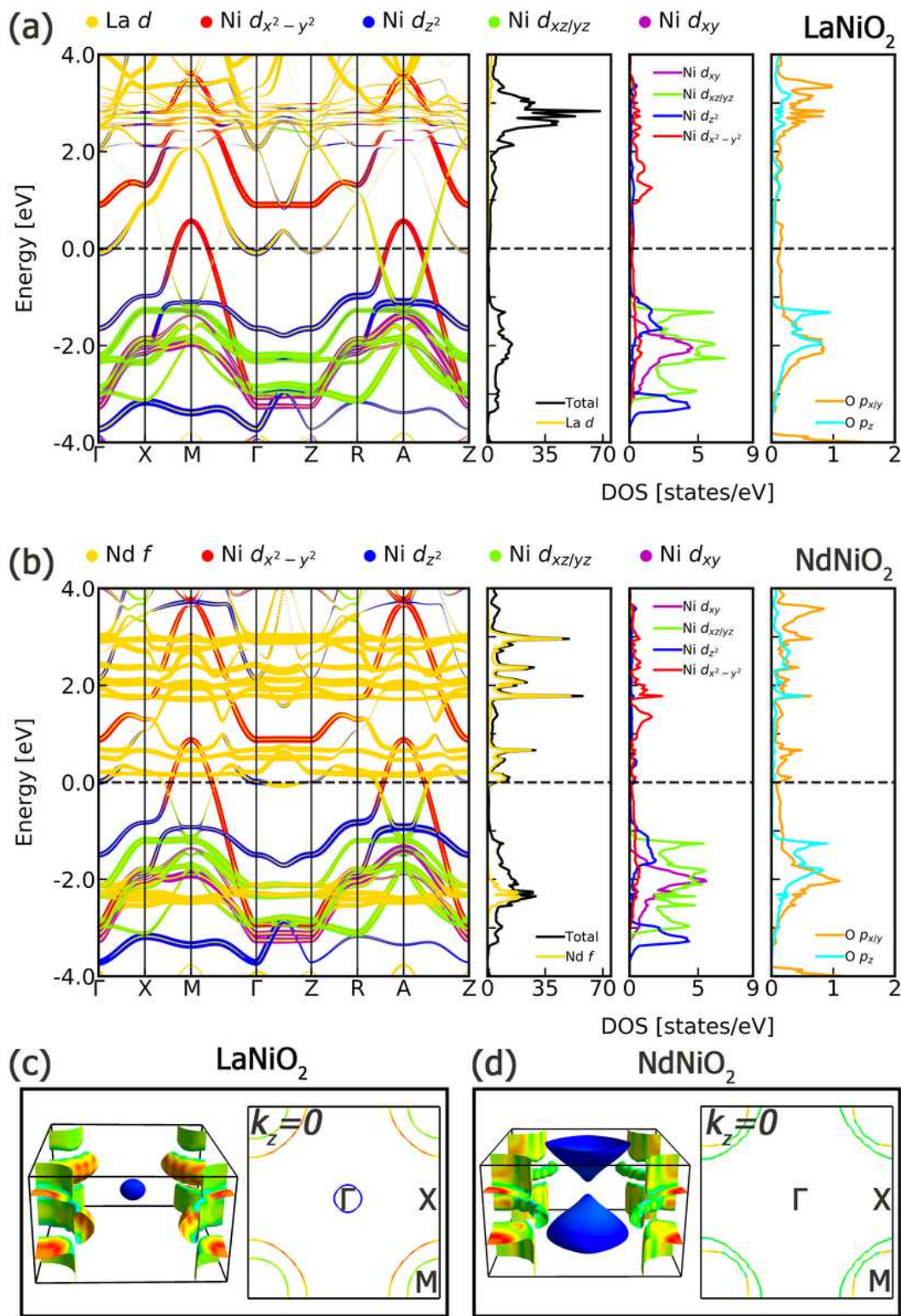


Figure 6

Orbital projected electronic structures of A-AFM phase of (a) LaNiO₂ and (b) NdNiO₂. The band structures are unfolded to the primitive $1 \times 1 \times 1$ BZ. (c) The calculated Fermi surface of LaNiO₂ and the projection of Fermi surface on the $k_z = 0$ plane. (d) Same as (c) but for NdNiO₂. Red, green, and blue indicate the maximum, middle, and minimum Fermi velocity, respectively.

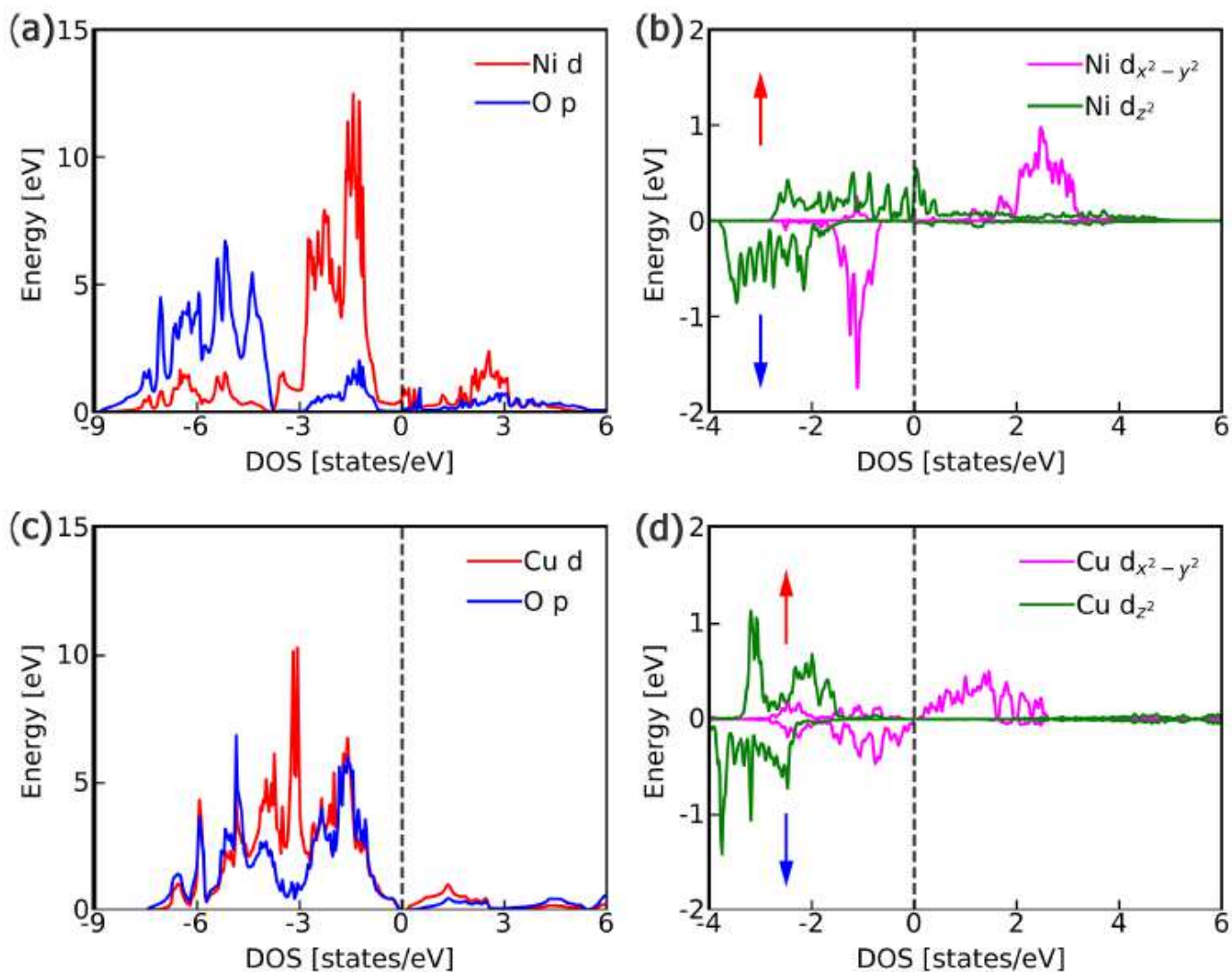


Figure 7

(a) Partial densities of states in the C-AFM phase of NdNiO₂, where red and blue lines represent the Ni *d* and O *p* orbitals, respectively. (b) Single nickel-site-resolved partial densities of states in the C-AFM phase of NdNiO₂, where the magenta and green lines represent the Ni $3d_{x^2-y^2}$ and $3d_{z^2}$ orbitals, respectively. And, the red and blue arrows represent the spin up and spin down channels, respectively. (c) and (d) same as (a) and (b), except that these panels refer to the C-AFM phase of CaCuO₂.

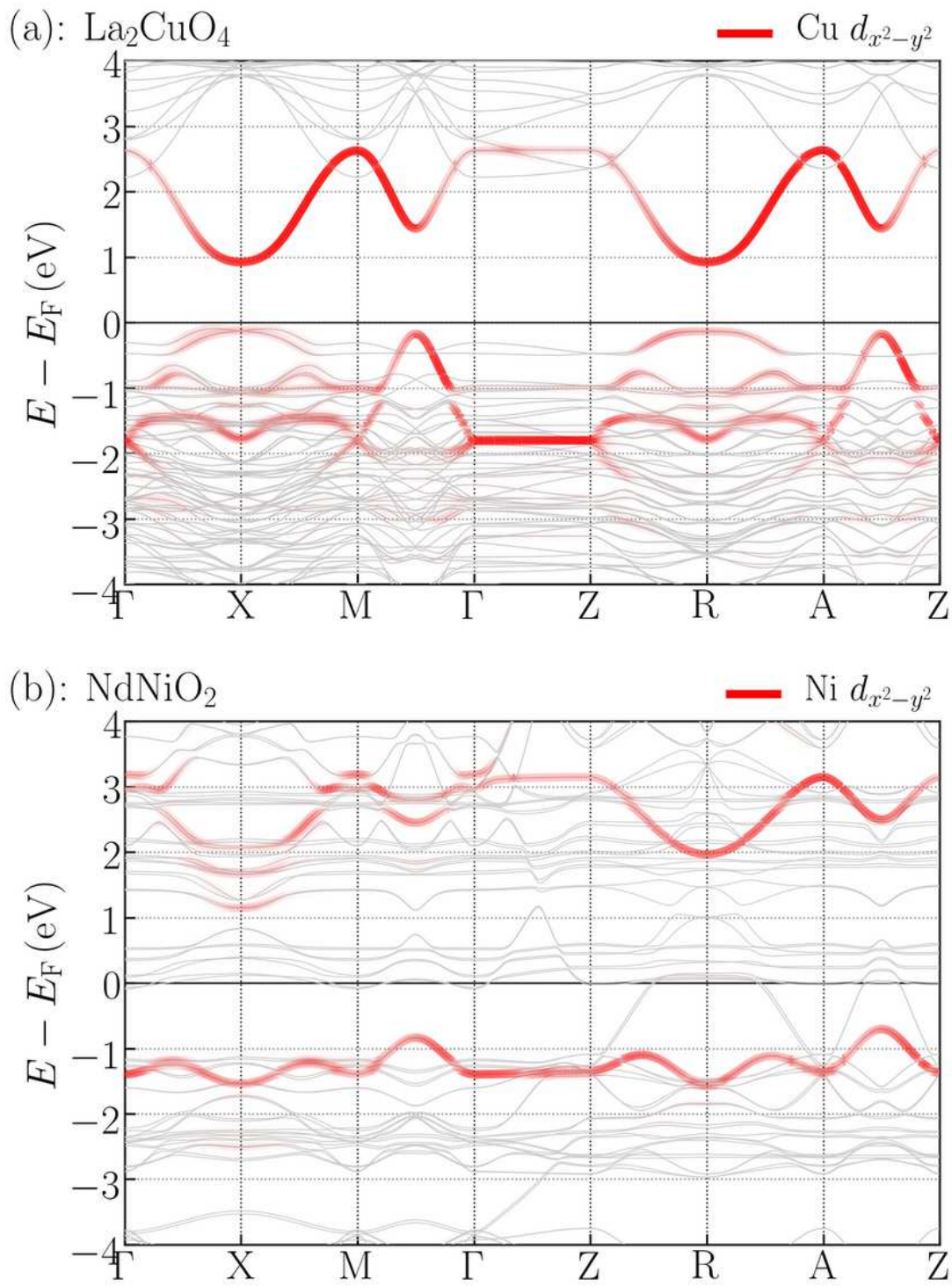


Figure 8

(a) Cu $3d_{x^2-y^2}$ band for G-AFM La_2CuO_4 . (b) Ni $3d_{x^2-y^2}$ band for C-AFM NdNiO_2 . Band structures have been unfolded into the $1 \times 1 \times 1$ primitive BZ.